PHYSICAL REVIEW B **81**, 205204 (2010)

Valence band study of thermoelectric Zintl-phase $SrZn_2Sb_2$ and $YbZn_2Sb_2$: X-ray photoelectron spectroscopy and density functional theory

Espen Flage-Larsen
Department of Physics, University of Oslo, P.O. Box 1048, Blindern, NO-0316 Oslo, Norway

Spyros Diplas
SINTEF Materials and Chemistry, P.O. Box 124, Blindern, Forskningsveien 1, N-0314 Oslo, Norway
and Chemistry Department, Centre for Materials Science and Nanotechnology (SMN), University of Oslo,
P.O. Box 1033, Blindern, Oslo 0315, Norway

Øystein Prytz
Department of Physics, University of Oslo, P.O. Box 1048, Blindern, NO-0316 Oslo, Norway

Eric S. Toberer
Materials Science, California Institute of Technology, Pasadena, California 91125, USA

Andrew F. May
Department of Chemical Engineering, California Institute of Technology, Pasadena, California 91125, USA

(Received 13 August 2009; revised manuscript received 15 March 2010; published 10 May 2010)

The electronic structure of $SrZn_2Sb_2$ and $YbZn_2Sb_2$ is investigated using density functional theory and high-resolution x-ray photoemission spectroscopy. Both traditional Perdew-Burke-Ernzerhof and state-of-the-art hybrid Heyd-Scuseria-Ernzerhof functionals have been employed to highlight the importance of proper treatment of exchange-dependent Zn $3d$ states, Yb $4f$ states, and band gaps. The role of spin-orbit corrections in light of first-principles transport calculations are discussed and previous claims of Yb^{3+} valence are investigated with the assistance of photoelectron as well as scanning and transmission electron microscopy.

DOI: 10.1103/PhysRevB.81.205204 PACS number(s): 71.15.Mb, 72.20.Pa, 74.25.F−, 78.70.En

I. INTRODUCTION

Thermoelectric materials allow the conversion of temperature gradients to electrical currents (and visa versa) without the need of moving parts. Thermoelectrics are appealing compared to conventional heat engines or compression-based refrigeration due to their scalability, noise-free operation, increased robustness, and improved integration. However, thermoelectric materials have seen limited applications due to their low efficiency. The figure of merit $zT = \alpha^2 \sigma T / \kappa$ is used to determine the efficiency of thermoelectric materials. A prerequisite for acceptable efficiency is a large Seebeck coefficient α, a large electrical conductivity σ, and at the same time, a small thermal conductivity κ. Based on traditional considerations, it is believed that the collection of materials that fulfill these properties is limited due to the interdependence of these three variables.[1]

The Zintl class of materials have recently gained significant interest due to their high thermoelectric efficiencies,[2] and significant effort is put into the search for common underlying principles among these materials.[2–5] Many of the Zintl materials contain heavy elements, which have localized d and f states, and it is thus difficult to predict properties based on first-principles calculations. In addition, the thermoelectric Zintl structures are often very complex (e.g., clathrates and 14-1-11 compounds).

One specific class of Zintl thermoelectric materials is however particularly simple, the AB_2Sb_2 ($P\bar{3}m1$, structure shown in Fig. 1) compounds. These compounds are thus attractive for detailed analysis. Within this material class, the thermoelectric performance has been assessed for different combinations of A=Sr, Ca, Yb, and Eu and B=Zn, Cd, and Mn. Peak values of zT have been reported between 0.4 and 1.2.[4,6–8] The A sites are formally 2+ cations while the $(B_2Sb_2)^{2-}$ network is covalently bounded slabs separated by cationic layers. The B site has tetrahedral coordination. Further studies of the detailed bonding and electronic transport may provide insight into the source of the varying thermoelectric performance among the AB_2Sb_2 compounds.

Thanks to the increased computational resources, more accurate hybrid functionals have been implemented in density functional theory (DFT) codes. These functionals partly correct the delocalization error by including a fixed portion of the Fock exchange term. Delocalization errors become particularly noticeable for d and f states, which are important for a wide range of the Zintl compounds. In particular, the f states are usually located close to the Fermi level and can be of great importance to the thermoelectric performance. One of the new hybrid functionals, the Heyd-Scuseria-Ernzerhof (HSE03) (Ref. 9) has shown excellent compromise between accuracy and speed.[10,11] This motivates us to compare calculations based on the HSE03 functional to previous calculations of these compounds, handled by traditional functionals and semiempirical modified Hubbard U models.[4,6]

Previous x-ray photoelectron spectroscopy (XPS) work on Yb-containing Zintl compounds showed presence of Yb^{3+}, which was claimed to be partly due to surface oxidation.[12–14] However, the previous study of the $YbZn_2Sb_2$ (Ref. 13) com-

©2010 The American Physical Society

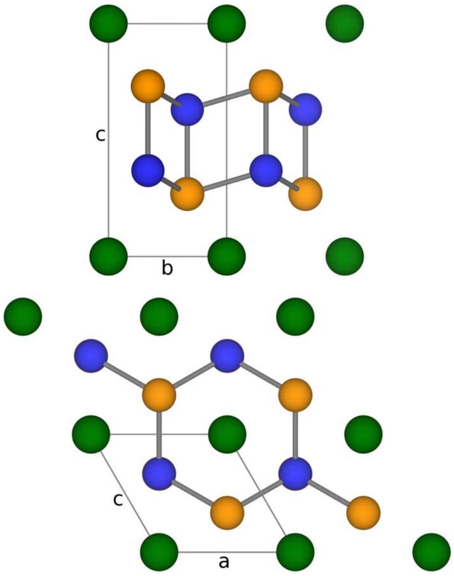

FIG. 1. (Color online) Zintl $AB\mathrm{Sb}_2$ compound in the $P\bar{3}m1$ space group. The *A* and *B* sites are green (darkest) and blue (dark), respectively. The Sb site is orange (light). The tetrahedral-coordinated *B* site and the tilted rectangular *B*-Sb network are illustrated.

pound did not address how the surface contamination affected the XPS spectra. Such studies are important to determine whether there is inherent Yb^{3+} in the compound or if the Yb^{3+} is a result of oxidation.

In this paper, we discuss the valence band spectra of the Zintl compounds $\mathrm{SrZn}_2\mathrm{Sb}_2$ and $\mathrm{YbZn}_2\mathrm{Sb}_2$ by comparing x-ray photoemission spectra and density functional calculations based on different functionals. In doing so, this study highlights the delocalization errors and the spin-orbit corrections. We also investigate the XPS spectra at different surface conditions to shed light on the importance of surface oxidation and show density of states calculations for the Yb^{3+} oxide $\mathrm{Yb}_2\mathrm{O}_3$. Scanning electron microscopy (SEM) and transmission electron microscopy (TEM) studies were also performed to further investigate oxidation effects, specifically whether oxide is present in the bulk of the sample.

II. METHODOLOGY

A. Sample preparation

Stoichiometric amounts of high-purity Zn (99.99%), Sb (99.999%), Yb (99.9%), and Sr (99.9%) were combined in a pyrolitic BN crucible (within an argon dry box), which was sealed in a quartz tube evacuated to 1×10^{-5} torr. Note that the elemental purity implies the metal basis purity. Samples were held at 1223 K for 30 min after a slow heating process. Cooling to 825 K took place over 2.5 h, at which point a 2.5 h anneal was employed. The resulting ingot was ball milled for 15 min in the high-energy SPEX 8000 Series Mixer/Mill utilizing stainless steel vial and balls (all steps under argon). Samples were consolidated via hot pressing at 823 K for ~3 h. A high-density graphite die (POCO) was employed and a force of roughly 1.4 t that was placed on a 12 mm diameter. The consolidated pellets were sliced using non-aqueous lubricant and the resulting wafers were ~1–2 mm thick.

B. X-ray photoemission spectroscopy

XPS valence band spectra were acquired in a Kratos Axis UltraDLD spectrometer. Prior to the analysis, the samples were polished and immediately submerged in ethanol (99.5 vol %). They remained in ethanol during transfer to the spectrometer in order to avoid extensive oxidation of the surface. The samples were taken out of the solution inside a glove box attached to the spectrometer, flashed with Ar for several hours and dried in a stream of Ar gas prior to their insertion in the fast entry chamber without being in contact with air. The XPS analysis was performed in a vacuum of 2×10^{-8} torr using Al $K\alpha$ radiation ($h\nu=1486.6$ eV) at 10 mA and 15 kV after Ar^+ sputtering of the sample surface. The valence band spectra were acquired at a pass energy of 5 eV and a step size of 0.05 eV. Survey scans were acquired at a pass energy of 160 eV and step size of 1 eV while for the core levels, we used a pass energy and a step size of 20 eV and 0.1 eV, respectively.

C. Scanning and transmission electron microscopy

The ytterbium sample was prepared for scanning electron microscopy (SEM) by submerged polishing in dry alcohol before it was put into a FEI Quanta 200 FEG-SEM for analysis. Spot energy-dispersive spectroscopy (EDS) spectra were acquired to map the sample composition. The material was further studied in a JEOL 2010F TEM after sample preparation using standard ion milling.

D. Density functional calculations

DFT calculations were based on Perdew-Burke-Ernzerhof (PBE) (Ref. 15) in the generalized gradient approximation (GGA), HSE03,[9] and the modified Perdew-Burke-Ernzerhof (PBE0) (Ref. 16) exchange-correlation functionals. Both hybrid functionals (HSE03 and PBE0) were evaluated within GGA. The projector-augmented-wave (PAW) (Refs. 17 and 18) method was employed. All calculations were done using a version of the Vienna *ab initio* simulation package (VASP) (Refs. 18–22) where the hybrid functionals are implemented. An energy cutoff of 550 eV and a Γ-centered *k*-point sampling of $10\times10\times6$ were sufficient to converge all results to within 1–2 meV for both $\mathrm{SrZn}_2\mathrm{Sb}_2$ and $\mathrm{YbZn}_2\mathrm{Sb}_2$. A Gaussian smearing of 0.3 eV (fitted to the Zn *d* peak width within the XPS spectra) was added to the calculated density of states where comparisons were done to the experimental spectra.

The electronic structure of $\mathrm{Yb}_2\mathrm{O}_3$ was calculated on a $4\times4\times4$ *k*-point grid using 750 eV as an energy cutoff with the PBE functional. All calculated density of states and band gaps were determined from a second run using the modified linear tetrahedron method.

The PBE0 functional is defined as

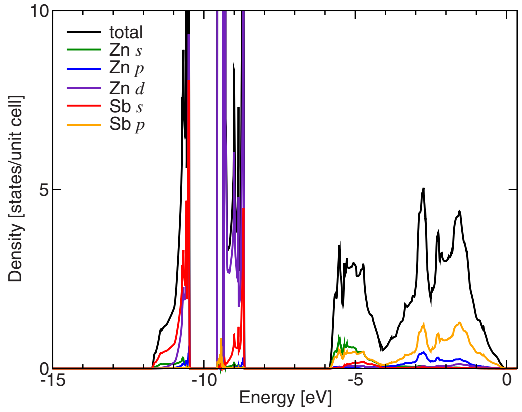

FIG. 2. (Color online) $SrZn_2Sb$ DFT projected density of states using the HSE03 functional.

$$E_{\mathrm{PBE0}} = \frac{1}{4}E_x^{\mathrm{HF}} + \frac{3}{4}E_x^{\mathrm{PBE}} + E_c^{\mathrm{PBE}}, \tag{1}$$

where the subscripts (x) and (c) term the exchange and correlation parts, respectively. The quarter mixing ratio is based on work done by Ernzerhof and co-workers.[23–25] The superscript signalizes how to evaluate the given energy, where HF is the Hartree energy and the exact exchange (this is thus the well-known Hartree-Fock[26] contribution). The PBE superscript tells us that the exchange and correlation should be evaluated from the PBE functionals. Similarly one can define range-separated hybrid functionals, like the HSE0y as

$$E_{\mathrm{HSE0}y} = \frac{1}{4}E_x^{\mathrm{HF,sr}} + \frac{3}{4}E_x^{\mathrm{PBE,sr}} + E_x^{\mathrm{PBE,lr}} + E_c^{\mathrm{PBE}}, \tag{2}$$

where (sr) and (lr) describe the short- and long-ranged parts of the exchange energy, respectively. This range separation is defined by separating the Coulomb kernel such that

$$\frac{1}{r} = \frac{\mathrm{erfc}(\mu r)}{r} + \frac{\mathrm{erf}(\mu r)}{r}, \tag{3}$$

where μ determines the range separation. For the HSE03 ($y=3$) functional, $\mu=0.3$ Å^{-1}. Such range separation is primarily motivated by the possibility of reducing the k-point grid[27] during the evaluation of the orbitals, which decreases the computational cost. Recent reviews of the hybrid functionals reveal a very good compromise between accuracy and performance for a wide range of benchmark systems.[11,27,28] Although, dependent on implementation and type of system, an order of magnitude increase in computational cost has to be expected over the traditional local-density approximation and GGA functionals.

III. RESULTS AND DISCUSSION

A. $SrZn_2Sb_2$

The projected density of states in the valence band is shown in Fig. 2 (results for HSE03, PBE is similar except for energy shifts, see later discussions). In the calculated upper valence band, Zn and Sb p states are predominant from 0 to −4 eV, where Zn p states fall off and an increased contribution of Zn s states is observed between −4 and −6 eV. The Zn d states are found as narrow bands around −10 eV, along with some hybridization with Sb s and p states. A similar electronic-structure results with the PBE functional. However, the common[29] underestimation of the Zn d-state binding energy occurs, leading to peak Zn d states being located at about −7.4 eV. Comparing these density of states calculations to the experimental XPS spectra in Fig. 3(a), better agreement is found with the HSE03 functional than the traditional PBE or PBE+U (Ref. 4) approach. Due to lack of sufficient XPS resolution compared to DFT, detailed comparison of Zn p and Sb p states close to the Fermi level cannot be done. However, the main Zn d-state peak and the trailing peak can be more closely examined.

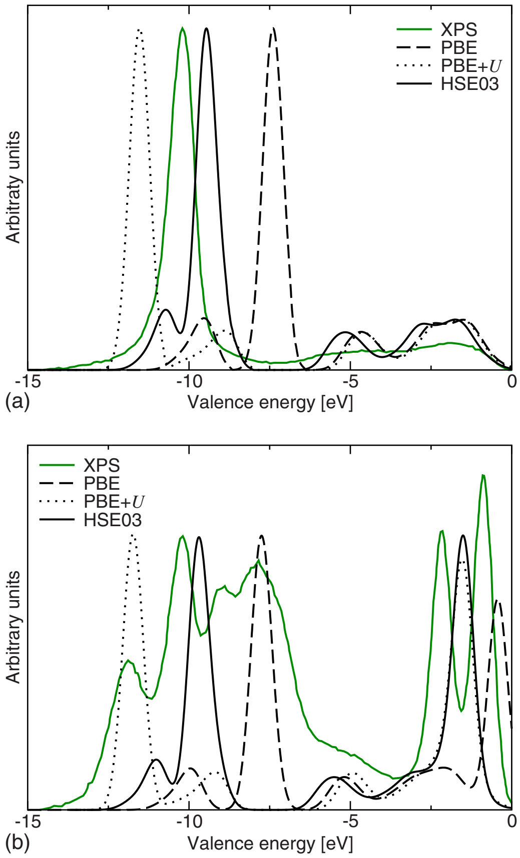

FIG. 3. (Color online) (a) $SrZn_2Sb$ and (b) $YbZn_2Sb_2$ DFT density of states for the HSE03 and the PBE functional and the PBE +U approach used in Ref. 4. The XPS spectra are also given.

The success of the HSE03 functional in determining the Zn d-state binding energy, and pulling the trailing Zn d and Sb s states to the main Zn d-state peak, arises from the inclusion of semilocal Fock terms in the functional. The main Zn d peak is shifted from −7.4 eV for the PBE calculation to −9.5 eV for the HSE03 calculation, a deviation of only 0.7 eV from the XPS results. These shifts are expected from the delocalization corrections, which mainly affect d and f states due to their spatial localization and thus increased Coulomb interaction. Corrections to the s states are smaller, consequently decreasing the energy separation between the main Zn d peak and the trailing Zn d and Sb s peak. A Gaussian

TABLE I. Calculated band gaps of $SrZn_2Sb_2$ and $YbZn_2Sb_2$ compounds using the PBE, HSE03, and PBE0 (not calculated for $YbZn_2Sb_2$) functional within the framework of density functional theory. Experimental thermal band gaps are previously determined (Refs. 4 and 8) from high-temperature Seebeck data (Ref. 31). Values are given in electron volt units.

Functional	$SrZn_2Sb_2$	$YbZn_2Sb_2$
PBE		
HSE03	0.21	0.16
PBE0	0.86	n/a
GGA+U	0.05	
Expt.	0.27	>0.15

smearing of 0.3 eV was applied to the calculated density of states but it is expected that the XPS s states are less resolved due to the small photoemission cross section of the s electrons. This leads to a relative difference between the experimentally observed s and d states that is not reflected in the calculations, and hence, no resolved peak is found to the left (higher binding energies) of the Zinc d peak as seen in the calculations. The incorporated long-range Fock terms in the PBE0 functional (not shown) shifts the Zn d peak to −9.7 eV, which is similar to the HSE03 result. Such small change is expected due to the semilocal sensitivity of these states.

The hybrid functionals also provide significant corrections to the band gap. In Table I, we summarize the results of the calculated band gaps for the respective functionals and compare against the thermal band gap estimated from the peak Seebeck coefficient.[4] The HSE03 functional again shows excellent corrections while PBE0 overcorrects, a result well known from pure Hartree-Fock calculations (for which the PBE0 functional is more similar than the HSE03 functional).

The features of the decomposed density of states close to the Fermi level are similar between the PBE and the HSE03 functional, except for the gap opening [see Fig. 4(a)]. In the p-type transport region, Sb p and Zn d states are the most important, which is in agreement with previous PBE+U work.[4]

Regardless of functional used, our calculations do not include spin-orbit coupling, which, for the free Zn atom, splits the d states into a $d_{3/2}$ and a $d_{5/2}$ peak, separated by ~0.1 eV.[30] In these materials, Zn is tetrahedral coordinated and should split into the well-known e_g and t_{2g} orbitals. This split was investigated and found to be around 0.1 eV, similar to the expected spin-orbit split of the free-atom Zn d states. The Gaussian smearing of 0.3 eV needed to match the width of the Zn d XPS peak would hide these effects (i.e., spin-orbit and crystal-field splits). Due to the hybridization between Zn d and Sb p states [see Fig. 3(a)], spin-orbit correction of the Zn d states would lift the Sb p states by at most 0.05 eV (based on the expected split of the free-atom values[30]).

The main reason for employing a PBE+U model in the previous study[4] was to open a small gap by shifting the Zn d states to higher binding energies. This reduced the Zn s binding energies due to increased Coulomb interaction. As a consequence, a small gap opened due to an upward shift of Zn s states in the lower conduction band. Even though a U value of 10 eV for the Zn d states only open a gap of 0.05 eV (see Table I), the Zn d peak is shifted to higher binding energies [see Fig. 3(a)] than what is observed in the XPS spectra. Increasing U further would worsen this disagreement. Thus, such models should be avoided unless they are used for a specific purpose in an isolated region of the energy spectrum with close consideration of XPS data.

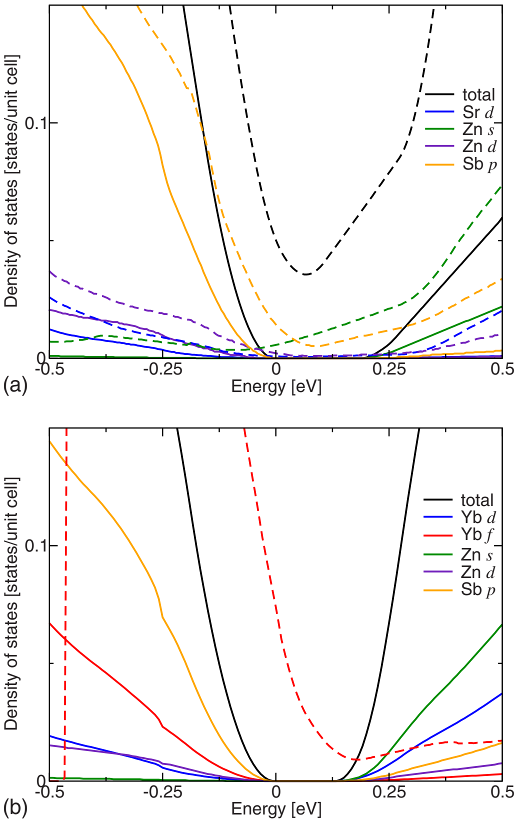

FIG. 4. (Color online) (a) $SrZn_2Sb$ and (b) $YbZn_2Sb_2$ DFT density of states close to the Fermi level. Solid and dashed lines are calculations with HSE03 and PBE functionals, respectively.

B. $YbZn_2Sb_2$

The main difference in the valence region (−15 to 0 eV) between $SrZn_2Sb_2$ and $YbZn_2Sb_2$ is expected to be the addition of Yb, and hence the Yb f valence states close to the Fermi level. This is observed in Fig. 3(b), where the f levels show up in both the calculated density of states and the experimental spectra. The previous discussion of the Zn states is very similar for this compound. No band gap is obtained for the PBE functional while the HSE03 functional opens a small gap (see Table I). In Fig. 4(b), the Yb f states calculated with the PBE functional and the HSE03 decomposed density of states are shown. The PBE-calculated Yb f states extend well into the gap while the binding energy of these states are increased in the HSE03 calculations, assisting the band-gap opening.

By comparing Figs. 4(a) and 4(b), a change in Sb p-state density is observed between the Sr and the Yb compound which is compensated (the total is very similar) by the addition of Yb *f* states.

From the XPS results in Fig. 3(b), the split of the Yb *f* states (∼1.3 eV) is similar to the free-atom separation of 1.2 eV.[30] Since no spin-orbit correction was included in the calculations, there is no split of the calculated Yb *f* states. The PBE functional is not in agreement with the XPS spectra, by placing the Yb *f* levels well past the Fermi level. The XPS results show that the edge onset should not extend far past the Fermi level. Similar trends between the PBE and HSE03 functionals in other Zintl compounds containing Yb (Refs. 6, 32, and 33) are expected. The HSE03-calculated Yb *f* peak fits well with the XPS results (if free-atom spin-orbit split of ∼1.2 eV is applied to the calculated peak). Spin-orbit-corrected Yb *f* states would shift some of the *f* states to higher energies and thus modify the gap [see Fig. 4(b)]. The PBE+U approach[4] is similar to HSE03 and XPS results for the Yb *f* peak, thus confirming U=5.3 eV to be acceptable for characterizing Yb in $YbZn_2Sb_2$ near the Fermi level. However, failures appear deeper in the valence band that are similar for the $SrZn_2Sb_2$ compound.

Previous work[4] showed (also confirmed here) hybridization between Yb *f* and Sb *p* states. Therefore, it is likely that spin-orbit corrections would raise the energy of the Sb *p* states slightly (in addition to the Yb *f* states) close to the Fermi level and reduce the band gap. In addition, because of the flat Yb *f* bands, the density of states increase rapidly from the Fermi level and down into the top valence band. Due to the *p*-type nature of these compounds,[4] spin-orbit coupling will be important for the transport properties for the $YbZn_2Sb_2$ compound but less important for the $SrZn_2Sb_2$ compound.

C. Yb valence

In addition to the expected Zn *d* and Yb *f* peaks close to the Fermi level in Fig. 3(b), additional band features are present between −4 and −12 eV in the XPS spectra. They are not reproduced by the calculations (regardless of functional) or present in the Sr sample. It is thus reasonable to assume they are related to the Yb. Previous studies[12,13] of Yb-containing Zintl materials suggest that the additional features that appear from −6 to −12 eV are due to Yb^{3+} valence, contradicting the expectation that Yb valence should be purely Yb^{2+} in these compounds. In Fig. 6(a), a peak fit[34] of the Yb 4*d* high-resolution spectrum confirms the presence of Yb^{3+}.

Based on the available structure data of compounds containing Yb, O, and/or Zn and Sb, oxidation of Yb would most likely form Yb_2O_3 and thus generate Yb^{3+} valence if it was not inherent in the structure. In Fig. 5(b), we show the calculated (PBE functional) valence band of Yb_2O_3. Even though the PBE functional is known to fail in oxides, the corrections usually give energy shifts due to delocalization and correlation corrections (and accordingly band-gap corrections). However, from Fig. 5(b), we see that even with a large energy shift, the proposed Yb^{3+} features in Fig. 3(b) are not reproduced. A direct comparison of calculated ground-state valence band and XPS spectra is not completely valid as the XPS spectra include additional excitations. For instance, the Yb^{3+} signature of Yb_2O_3 was suggested to be a consequence of 4*d*-4*f* resonances.[35] The Yb^{3+} presence due to Yb_2O_3 was also indicated in a previous x-ray diffraction and XPS study[13] of this compound but neither direct proof nor explicit data of the oxygen content was given.

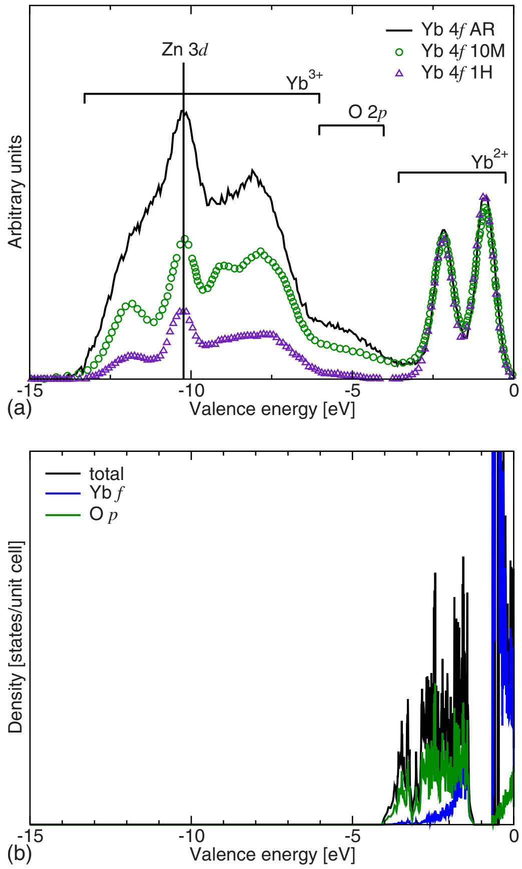

FIG. 5. (Color online) (a) Top valence XPS spectra of $YbZn_2Sb_2$ for three different Ar^+ sputtering events. (b) Calculated density of states for the Yb_2O_3 oxide using the PBE functional.

To further investigate the surface oxidation, the XPS spectra of the Yb 4*d* and the top valence region of $YbZn_2Sb_2$ have been acquired after three different *in situ* sputtering events, see in Figs. 6(a) and 5(a), respectively. The as-received sample shows large Yb^{3+} contributions compared to the Yb^{2+}. Increasing the sputtering time clearly reduces the Yb^{3+} contributions significantly in the acquired spectra. The 4*d* spectra were normalized by aligning the Yb^{2+} component with the lowest binding energy. In the top valence band, the spectra were normalized to the Yb^{2+} peaks. A clear correlation can be seen between the reduction in Yb^{3+} and O 1*s* peaks in Fig. 6(b) when the sputter time increases. The large peaks at −532 and −541 eV is most likely a form of Sb oxide on the surface. These peaks are removed during Ar^+ sputtering. The relatively strong XPS features from −4 to −6 eV are caused by O *p* states (downshift of these is expected in, e.g., HSE03 calculations) as indicated in Fig. 5(b) and from the strong correlation with sputtering time [see Fig. 5(a)].

However, even though the contribution of oxygen decreases as sputtering time increases, there are still Yb^{3+} fea-

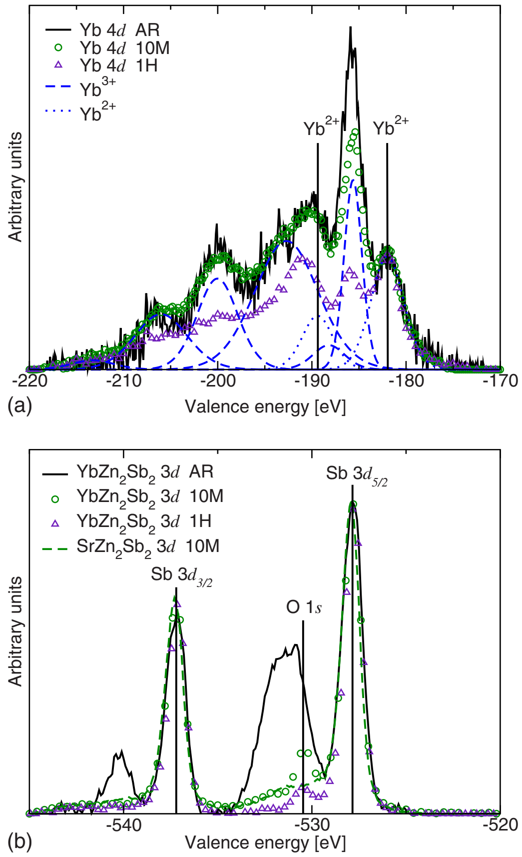

FIG. 6. (Color online) (a) Peak fitting of Yb 4*d* spectrum. Three different XPS spectra are included, where AR, 10M, and 1H is sample as received, sputtered for 10 min and 1 h, respectively. Vertical lines highlight the contribution of Yb^{2+}. All other peaks are due to the Yb^{3+} contribution. Peak fitting was performed according to previous work (Ref. 34). The background was subtracted according to the Shirley method (Ref. 36). (b) The Sb 3*d* and O 1*s* peaks of $YbZn_2Sb_2$ and $SrZn_2Sb_2$.

tures in the XPS spectra. This is likely caused by either Yb_2O_3 oxide in the grain boundaries or inherent stimulated Yb^{3+} valence due to defects or superstructures. The Zn *d* peak also decreases but this is expected due to the overlap with the Yb^{3+} signal.

To shed more light on the Yb valence issues, we performed SEM and TEM. The SEM analysis revealed grains of different sizes, where a significant presence of oxygen was detected inside and along the grain boundaries. The larger grains were oxygen free within the resolution of the SEM EDS analysis. TEM studies revealed small particles, 30–60 nm in size, embedded in the bulk material matrix. EDS analysis performed on the TEM confirmed that these particles are oxygen rich compared to the matrix, see Fig. 7.

We also investigated the possibility for a simple superstructure by relaxing (with no symmetry restrictions) a $1 \times 1 \times 3$ supercell. No significant change in occupancy was found between the respective Yb layers. In addition, we performed a relaxation of the same supercell but with one Yb removed. Even though small charge variances were observed and no clear Yb^{3+} formation was detected around the defect. All results thus point to formation of Yb_2O_3 in the grain boundaries as the likely reason for the residual Yb^{3+} signature.

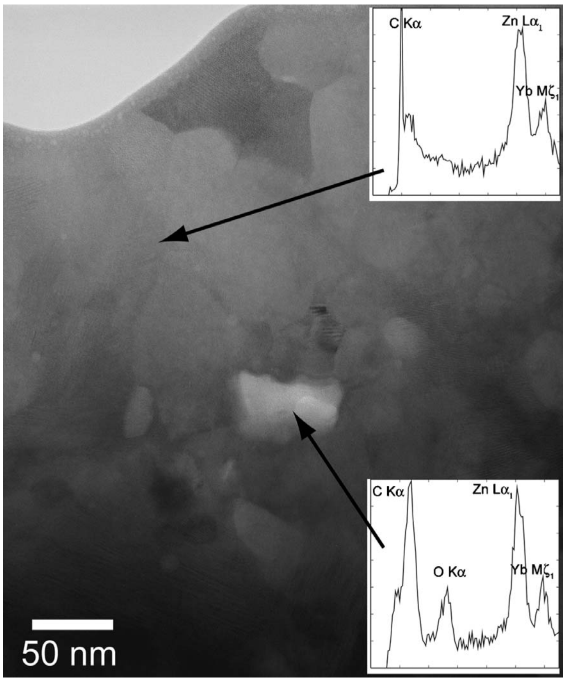

FIG. 7. Bright-field TEM micrograph of an oxygen-rich particle embedded in the matrix. The insets are EDS spectra confirming the increased amount of oxygen in the particle.

A previous Zintl study[12] proposed inherent Yb^{3+} in the $Yb_{14}ZnSb_{11}$ but not in the $Yb_{14}MnSb_{11}$ compound. They claimed that the Yb^{3+} signal was significantly enhanced in the Zn-containing compound. However, the Zn *d*-state peak appears in the same region, such that the difference between the Mn and the Zn-containing structure could be related to absent Zn *d* states and not necessarily presence of Yb^{3+}. Even though the two compounds are different, it is however likely that the detected Yb^{3+} valence of these compounds could similarly stem from grain-boundary oxidation during synthesis processes.

IV. SUMMARY AND CONCLUDING REMARKS

In this work, we studied the valence band and band gaps of Zintl $SrZn_2Sb_2$ and $YbZn_2Sb_2$ compounds by comparing density functional calculations and XPS spectra. The hybrid HSE03 functional was shown to give significant and important corrections over the traditional PBE functional, such as size of band gap and placement of Yb *f* levels which will be of utmost importance when first-principles transport calculations are to be done based on the band structure. Due to the delicate balance between speed and accuracy, the HSE03 functional will most likely serve as an excellent base for transport calculations of the rare-earth-based thermoelectric materials if spin-orbit corrections are included. The semi-empirical PBE+U and its variants should be used with care and compared to experimental spectra to confirm the choice of U (and J for models where it applies). We also investigated the previously reported Yb^{3+} signature. A strong correlation between sputtering time and the Yb^{3+} peak intensities was found, supporting severe surface Yb_2O_3 contamination. However, even after one hour of sputtering, the Yb^{3+} peaks were still present (although the O 1*s* peak was strongly reduced). This implied questions regarding the structure, e.g., whether superstructures or defects could be largely present in the $YbZn_2Sb_2$ samples. It could also indicate that Yb_2O_3 oxide is inherent in the sample and not strictly a surface effect. Superstructure and defect calculations suggested Yb_2O_3 in the grain boundaries to be the likely explanation, which was confirmed by SEM and TEM analysis.

ACKNOWLEDGMENTS

Espen Flage–Larsen would like to thank the Norwegian Research Council for financial support and the NOTUR project for computational resources. Øystein Prytz would also like to thank the Norwegian Research Council for funding. In addition, we would like to thank Ole Martin Løvvik and Ole Bjørn Karlsen for discussions.

---

[1] G. J. Snyder and E. Toberer, Nature Mater. **7**, 105 (2008).
[2] S. M. Kauzlarich, S. R. Brown, and G. J. Snyder, Dalton Trans. **21**, 2099 (2007).
[3] B. C. Sales, D. Mandrus, and R. K. Williams, Science **272**, 1325 (1996).
[4] E. S. Toberer, A. F. May, B. C. Melot, E. Flage-Larsen, and G. J. Snyder, Dalton Trans. **39**, 1046 (2010).
[5] E. S. Toberer, A. F. May, and G. J. Snyder, Chem. Mater. **22**, 624 (2010).
[6] X.-J. Wang, M.-B. Tang, H.-H. Chen, X.-X. Yang, J.-T. Zhao, U. Burkhardt, and Y. Grin, Appl. Phys. Lett. **94**, 092106 (2009).
[7] T. J. Z. C. Yu, S. N. Zhang, X. B. Zhao, J. He, Z. Su, and T. M. Tritt, J. Appl. Phys. **104**, 013705 (2008).
[8] F. Gascoin, S. Ottensmann, D. Stark, S. M. Haile, and G. J. Snyder, Adv. Funct. Mater. **15**, 1860 (2005).
[9] J. Heyd, G. E. Scuseria, and M. Ernzerhof, J. Chem. Phys. **118**, 8207 (2003).
[10] J. L. F. Da Silva, M. V. Ganduglia-Pirovano, J. Sauer, V. Bayer, and G. Kresse, Phys. Rev. B **75**, 045121 (2007).
[11] E. N. Brothers, A. F. Izmaylov, J. O. Normand, V. Barone, and G. E. Scuseria, J. Chem. Phys. **129**, 011102 (2008).
[12] A. P. Holm, T. C. Ozawa, S. M. Kauzlarich, S. A. Morton, G. D. Waddill, and J. G. Tobin, J. Solid State Chem. **178**, 262 (2005).
[13] O. Y. Zelinska, A. V. Tkachuk, A. P. Grosvenor, and A. Mar, Chem. Met. Alloys **1**, 204 (2008).
[14] A. Szytuła, A. Jezierski, B. Penc, M. Hofmann, and S. Campbell, J. Alloys Comp. **366**, 313 (2004).
[15] J. P. Perdew, K. Burke, and M. Ernzerhof, Phys. Rev. Lett. **77**, 3865 (1996).
[16] C. Adamo and V. Barone, J. Chem. Phys. **110**, 6158 (1999).
[17] P. E. Blöchl, Phys. Rev. B **50**, 17953 (1994).
[18] G. Kresse and D. Joubert, Phys. Rev. B **59**, 1758 (1999).
[19] G. Kresse and J. Furthmüller, Comput. Mater. Sci. **6**, 15 (1996).
[20] G. Kresse and J. Furthmüller, Phys. Rev. B **54**, 11169 (1996).
[21] G. Kresse and J. Hafner, Phys. Rev. B **49**, 14251 (1994).
[22] VASP code, http://cms.mpi.univie.ac.at/vasp
[23] M. Ernzerhof, Chem. Phys. Lett. **263**, 499 (1996).
[24] M. Ernzerhof, J. P. Perdew, and K. Burke, Int. J. Quantum Chem. **64**, 285 (1997).
[25] J. P. Perdew, M. Ernzerhof, and K. Burke, J. Chem. Phys. **105**, 9982 (1996).
[26] V. Fock, Z. Phys. **61**, 126 (1930).
[27] M. Marsman, J. Paier, and G. Kresse, J. Phys.: Condens. Matter **20**, 064201 (2008).
[28] J. Heyd and G. E. Scuseria, J. Chem. Phys. **121**, 1187 (2004).
[29] J. Uddin and G. E. Scuseria, Phys. Rev. B **74**, 245115 (2006).
[30] M. Cardona and L. Ley, *Photoemission in Solids I: General Principles* (Springer-Verlag, Berlin, 1960), with corrections.
[31] H. J. Goldsmid and J. W. Sharp, J. Electron. Mater. **28**, 869 (1999).
[32] S.-J. Kim, J. Salvador, D. Bilc, S. D. Mahanti, and M. G. Kanatzidis, J. Am. Chem. Soc. **123**, 12704 (2001).
[33] S. Bobev, V. Fritsch, J. D. Thompson, J. L. Sarrao, B. Eck, R. Dronskowski, and S. M. Kauzlarich, J. Solid State Chem. **178**, 1071 (2005).
[34] Y. Ohno, J. Electron Spectrosc. Relat. Phenom. **165**, 1 (2008).
[35] L. I. Johansson, J. W. Allen, I. Lindau, M. H. Hecht, and S. B. M. Hagström, Phys. Rev. B **21**, 1408 (1980).
[36] H. Tokutaka, N. Ishihara, K. Nishimori, S. Kishida, and T. Takabuchi, Jpn. J. Appl. Phys., Part 1 **29**, 2512 (1990).